The characterisation of upconversion nanoparticles by single particle ICP-MS employing a quadrupole mass filter with increased bandpass

Sarah Meyer [a], Raquel Gonzalez de Vega [a], Xiaoxue Xu [b], Ziqing Du [b], Philip A. Doble [a], David Clases [a,*]

[a] The Atomic Medicine Initiative, University of Technology Sydney, Sydney, NSW, Australia

[b] Institute for Biomedical Materials and Devices, Faculty of Science, University of Technology Sydney, NSW, 2007, Australia

[*] Corresponding author: **David.Clases@uts.edu.au**

ABSTRACT: This work introduces new methods to characterise dispersions of small or low mass fraction nanoparticles (NPs) by single particle – inductively coupled plasma – mass spectrometry (SP ICP-MS). The optimisation of ion extraction, ion transport and the operation of the quadrupole with increased mass bandwidth improved signal to noise ratios significantly and decreased the size detection limits for all NP dispersions investigated. As a model system, 10.9 ± 1.0 nm Au NPs were analysed to demonstrate the effects of increasing ion transmission. Specifically, increasing the mass bandwidth of the quadrupole improved size detection limits as low as 4.2 nm and enabled the resolution of NP signals from ionic background and noise. Subsequently, the methods were applied to the characterisation of lanthanide doped upconversion nanoparticles (UCNPs) by SP ICP-MS for the first time. Three different types of UCNPs (90 nm $NaYF_4$: 20%Yb, 2%Er; 20 nm $NaGdF_4$: 20%Yb, 1%Er; 15 nm $NaYF_4$: 20%Yb, 2%Er) were investigated. Y showed best signal to noise ratios with optimised ion extraction and transport parameters only, whereas the signal to noise ratios of Gd, Er, Yb were further improved by increasing the mass bandwidth of the quadrupole mass filter. The novel methods were suitable for detailed characterisation of diluted UCNP dispersions including particle stoichiometries and size distributions. A Poisson model was further applied to assess particle-particle interactions in the aqueous dispersions. The methods have considerable potential for the characterisation of low diameter and/or low mass fraction nanoparticles.

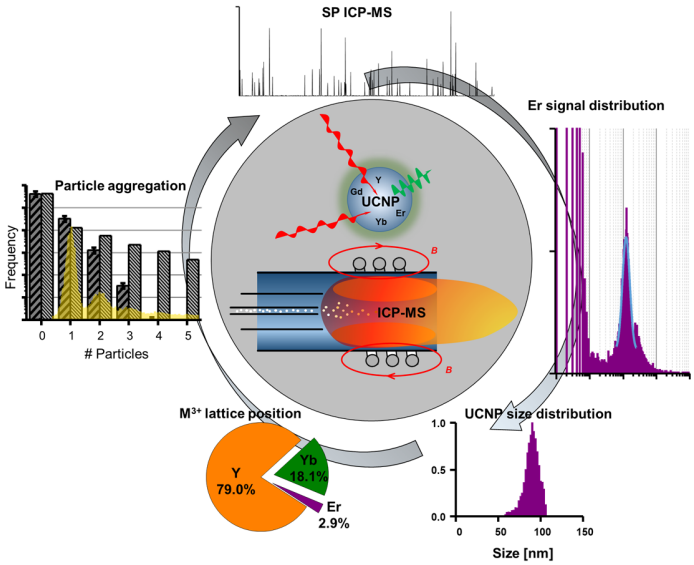

Graphical abstract. Characterisation of UCNPs via SP ICP-MS.

Keywords: single particle ICP-MS, SP ICP-MS, bandpass mass filter, Au nanoparticles, UCNP, size detection limit

INTRODUCTION

Nanomaterials comprise a large group of compounds containing structures on a scale between 1 and 100 nm and exhibiting properties that are quite different from their (non-nanostructured) bulk counterparts. They are attracting increasing interest as they can be exploited and customised for various chemical, biological, or physical applications. Nanoparticles (NPs) are useful for medicine, numerous research disciplines and industrial applications such as therapeutic agents, drug delivery, chemical sensors and probes, personal care products, catalysis, coatings and paints.[1–4] Their manufacture and application rely on methods to accurately and precisely characterise elemental compositions, size distributions and stability.[5,6]

Lanthanide doped upconversion nanoparticles (UCNPs) have unique optical, electronic, and magnetic characteristics. The doped lanthanide ions in the host crystal allow electronic transitions which can be harnessed for photon upconversion by consecutive absorption of low energy photons. This can be exploited for high-resolution microscopy, bio-sensing, solar energy harvesting, deep-tissue optical bio-imaging and multimodal diagnostics.[6–10] The optical properties of UCNPs are tuneable and depend on the selection, combination and amount

of doped lanthanide ions, the stoichiometry, host structure, density, and size.[11] The understanding, control, and prediction of properties of UCNPs require versatile and dedicated analytical methods.[12–15] For example, it is essential to accurately measure the number and size of dispersed UCNPs to ensure efficient surface modifications for conjugation when using biomolecules with different moieties, such as antibodies, ssDNA, or miRNA.[16] Furthermore, dispersion and chemical stability must be considered for practical clinic applications.

Inductively coupled plasma – mass spectrometry (ICP-MS) emerged almost four decades ago and is a multifaceted technique for elemental analyses over a vast linear dynamic range.[17] In combination with secondary instrumentation like liquid chromatography and laser ablation (LA), it is possible to perform speciation analysis and elemental bio-imaging of various metal species, including NPs.[18–23] The progressive instrumental advancements for rapid detection and improved processing algorithms have opened new strategies for detection and characterisation of individual NPs.[24–27] The principle of this *single particle* (SP)-ICP-MS relies on the individual detection of NPs in dilute dispersions. At low particle concentrations, NPs are individually transported into the ICP, where they are atomised prior to ionisation. The resulting ion cloud is extracted into the mass spectrometer to produce discrete signals when focused onto the detector.[28] Several thousand particles may be individually sampled per minute to calculate particle number concentrations and to construct models of size distributions and particle-particle interactions.[28–30] Ion transmission is relatively low in ICP-MS which limits the observable size of NPs. After atomisation, ionisation, ion extraction, ion transport and mass filtering, only a small fraction of isotopes per NP reaches the detector.[31] For particles with dimensions at the size detection limit (sDL), signals are within the standard deviation of the background signal, which is generated by ionic species of the targeted analyte and the electronic noise. This limits the applicability of SP ICP-MS for the measurement of small or low mass fraction particles.[32,33]

Despite its excellent potential for NP characterisation,[34] SP ICP-MS has not yet been applied to the investigation of UCNP dispersions. This is most likely related to small particle sizes and low concentrations of doped lanthanides requiring low sDL which are often beyond the capability of conventional SP ICP-MS. Methods improving ion transmission to increase signal to noise ratios in ICP-MS have the potential to overcome these limitations.[31,32] Different strategies to alter ion extraction, ion transport and mass filtering may be applied to increase ion transmission to improve the sDL and to bring small UCNPs within the reach of SP ICP-MS. Tuoriniemi *et al.* employed sector-field ICP-MS which increased ion transmission by operating with hard extraction conditions. The authors also suggested to use a jet interface to further improve transmission.[31] Similarly, Frechette-Viens *et al.* showed recently that sDL of Zn NPs can be increased by operating sector field-based ICP-MS.[35] Another option to improve ion transmission is the manipulation of the mass bandwidth of the quadrupole. Balcaen *et al.* employed ICP-MS/MS where the first quadrupole was operated with a large mass bandpass to allow the simultaneous transmission of S^+ and SO^+, whereas the third quadrupole was operated with unit mass resolution.[36] A similar strategy was followed to improve the signal to noise ratios of endogenous elements in LA-ICP-MS/MS.[37] Recently, we employed (single quadrupole) LA-ICP-MS and altered the mass bandwidth of lanthanides to increase signal to noise ratios for the analysis of metal labelled antibodies by a factor of 6.86 relative to a standard method.[38]

This work details the development and application of a new method to enhance ion transmission and to decrease the sDLs for UCNPs. As proof of concept, dispersions of small Au NPs (10.9 nm) were initially investigated to demonstrate how ion extraction and transport may be altered for the detection of small NPs. We further manipulated the mass bandpass in ICP-MS to increase the transmission of the quadrupole mass filter while decreasing mass resolution. These approaches were combined to determine size distributions, stoichiometry, and particle-particle interactions of lanthanide doped UCNPs.

MATERIALS AND METHODS

Chemicals and consumables

Ultrapure water was obtained from an Arium® pro system (Sartorius Stedim Plastics GmbH, Germany). The daily performance of the ICP-MS instrument was monitored using a tuning solution containing 1 µg L^{-1} Li, Y, Tl, Ce and Ba. The detector deadtime was determined by analysing diluted Er standards from High Purity Standards (SC, USA).

Au NP dispersions (NanoXact Nanospheres – Bare (Citrate), 99.99% purity) with diameters of 4.4 ± 0.5, of 10.9 ± 1.0 and 15 ± 1.3 nm were purchased from nanoComposix (CA, USA) in a 2 mM sodium citrate solution and stored at 4°C. Mass concentrations were determined by the supplier using ICP-MS (Thermo Fisher X Series 2). The diameter and size statistics were undertaken using ICP-MS JEOL 1010 Transmission Electron Microscope and a Malvern Zetasizer Nano ZS. Upon analysis, stock solutions were sonicated and diluted in containers made of polypropylene for SP ICP-MS. For the acquisition of mass spectra and elemental responses, certified Au, Y, Yb, Er and Gd standard solutions for ICP-MS were obtained at 10 µg mL^{-1} in 2 % HNO_3 from High Purity Standards and diluted to 1 ng mL^{-1} for analysis.

Three types of UCNPs were manufactured in-house using yttrium chloride hexahydrate ($YCl_3 \cdot 6H_2O$, 99.99%), ytterbium chloride hexahydrate ($YbCl_3 \cdot 6H_2O$, 99.998%), erbium chloride hexahydrate ($ErCl_3 \cdot 6H_2O$, 99.9%), gadolinium chloride hexahydrate ($GdCl_3 \cdot 6H_2O$, 99%) sodium hydroxide (NaOH, 98%), ammonium fluoride (NH_4F, 99.99%), oleic acid (OA, 90%), 1-octadecene (ODE, 90%), and hydrochloric acid (HCl, 37%). All reagents were purchased from Sigma-Aldrich and used as received without further purification.

UCNP synthesis and characterisation

Synthesis of UCNPs: The typical synthesis procedure for the $NaYF_4$ host UCNPs doped with lanthanide ions of Yb and Er was based on a study by Liu *et al.*.[39] The procedure for the $NaGdF_4$ host UCNPs doped with Yb and Er followed the protocol by Wang *et al.*.[40] Further information on the UCNP synthesis is given in the supplementary information. Samples were dispersed in cyclohexane for transmission electron microscopy (TEM) characterisation and stored at -20°C until further use. 0.1

M HCl solution was used to wash off the oleic acid from the UCNPs surface to disperse them in DI water for ICP-MS characterisation. To avoid potential UCNP dissolution, samples were immediately analysed after dispersion and dilution and cooled on ice during analysis.

UCNPs characterisation: TEM images of all three types of UCNPs were recorded with a FEI Tecnai T20 transmission electron microscope and are shown in Figure S1A (supplementary information). The dimensions and numbers of the nanoparticles were determined, counted, and graphed with ImageJ 1.50I software. Crystal phase analysis of nanoparticles was performed using a Bruker D8 Discover A25 X-ray diffractometer with Cu Kα1 radiation (40 kV, 40 mA, λ=0.15406 nm). The results were compared against the PDF-4+2019 RDB database to identify the crystal phase and structure (Figure S1B). In these cases, all UCNPs crystallised hexagonally, which allowed the calculation of UCNP densities according to Mackenzie *et al.*.[41]

SP ICP-MS analysis and experimental parameters

For SP ICP-MS, an 8900 series ICP-MS/MS system (Agilent Technologies) was equipped with Pt cones and s-lenses. The torch accommodated an injector with a diameter of 1.5 mm. Aerosols were generated via self-aspiration employing a concentric nebuliser and a Scott double pass spray chamber cooled to 2°C. The ICP-MS/MS was operated in SQ-mode and the dwell time of the quadrupole was set to 100 µs. Elements were monitored consecutively and with an acquisition time of 90 s and data analysis was performed using MassHunter software (Agilent Technologies) and OriginPro (OriginLab, Version 9). The RF power was set to 1.6 kW, the sample depth (z-position) to 8.0 mm, the nebuliser gas to 1.08 L min^{-1} for Au analysis and 1.04 L min^{-1} for lanthanide analysis. The oxide ratio ($^{157}Gd^{16}O^+/^{157}Gd^+$) was below 1.8%. The gradual optimisation to enhance transmission required modification of the ion optics and the quadrupole mass filter. Parameters for each acquisition mode are given in Table 1. Except for the bandpass mode, all masses were monitored at unit resolution with peak widths of 0.7 amu at 10% peak height, and Q1 was operated with a scanning line gain factor of 0.9. In bandpass-mode, mass resolution was decreased for both quadrupoles to increase ion transmission.

Table 1. Experimental parameters. The standard method featured soft extraction parameters. Based on this method, ion extraction and transport were optimised for Y, Au and lanthanides (optimised ion lenses). Finally, a bandpass mode employing the quadrupole as a bandpass filter was developed and applied to Gd, Er, Yb and Au.

	Standard method [V]	Optimised ion lenses [V]	Bandpass mode [V]
Extract 1	4.0	-200.0	-200.0
Extract 2	-230	-6.0	-6.0
Omega Bias	-150	-190	-200
Omega Lens	10.0	11.0	13.0
Cell Focus	0.0	-14.0	-17.0
Deflect	13	14	20

Data analysis

The elemental responses and mass spectra were obtained by analysing a certified ionic 1 µg L^{-1} standard for ICP-MS. Ultrapure water was analysed as a blank and the background intensity was subtracted. The rapid scanning of the quadrupole provided 4 data points on average per individual NP, and the resulting peaks were integrated and depicted in a histogram. For the size calibration of NPs, particle diameters were calculated on the basis of a previously analysed 15 ± 1.3 nm Au NP dispersion as custom reference material using MassHunter software, which were characterised by the supplier regarding mass concentration, particle number concentration and size distribution. For UCNPs, particle masses (m_p) and diameters (D_p) were calculated following equations 1-3 using MassHunter software. The sDL was calculated according to Lee *et al.* as shown in equation 4.[42]

$$\eta = \frac{N_m}{N_{th}} \quad (1)$$

$$m_p = \frac{I_p\, t_d\, V\, \eta\, f}{s} \quad (2)$$

$$D_p = \sqrt[3]{\frac{6 m_p}{\pi\, \rho_p}} \quad (3)$$

$$sDL = \sqrt[3]{\frac{6 \cdot 3\, \sigma_{DI}}{\pi\, \rho_p\, f\, R}} \quad (4)$$

Where η is the transport efficiency (11.0%) as the ratio of measured particles N_m and the theoretical number of particles N_{th} in a sampled volume. I_p is the measured particle signal (integrated area), t_d the dwell time (100 µs), V the sample inlet flow (350 µL min^{-1}), f the molar mass fraction, s the response factor of an 1 ng ml^{-1} ionic standard, ρ_p the particle density, and R the mass related response factor of a nanoparticle.[42] σ_{DI} is the standard deviation and was calculated from 225,000 integrations with integration intervals corresponding to the average NP signal duration (400 µs) of a blank (ultrapure water) solution. To improve the comparison of histograms, signal distributions were fitted using a log-normal distribution model. A Poisson distribution model was used to estimate the number of events where two or more particles were detected simultaneously.

RESULTS AND DISCUSSION

Maximising ion transmission

Due to relatively low ion transmission in ICP-MS, only a small fraction of ionised masses generated within the ICP reaches the detector. This limits the observable size of individual NPs in single particle mode as the corresponding signals become indistinguishable from background noise. Ion transmission may be improved by consideration of two aspects: optimisation of ion lenses' parameters to improve ion extraction and transport; and manipulation of quadrupole mass filtering. The former has been investigated in various studies and is accomplished by employing hard extraction conditions, which are applied in sector-field-based ICP-MS set-ups[31] but also in combination with cool and dry plasmas in quadrupole-based GC-ICP-MS[43] and LA-

ICP-MS[38]. During hard extraction, the polarity of the first extraction lens is reversed to highly negative potentials (e.g. -200V, Table 1) whereas the second extraction lens is operated closer to the ground potential (e.g. -6V, Table 1) increasing the kinetic energy of ions.[44] This results in a more efficient ion extraction and transport, which simultaneously mitigates space charge effects. However, increasing the kinetic energy of the extracted ions requires consideration of the potentials applied to the following ion lenses (e.g., omega lenses) to ensure maximum transmission. Table 1 lists the instrumental parameters of a standard method as well as a hard extraction method with modified ion lenses.

The transmission in quadrupole MS can be manipulated and increased at the expense of selectivity.[45] A quadrupole analyser is operated with a set of RF and DC voltages which stipulate stable trajectories for specific m/z ratios. The two-dimensional (x, y) motion of ions through the quadrupole can be described by the Mathieu equations and depends on the RF and DC voltages applied to the four metallic rods. The Mathieu equations are second order differential equations and can be solved numerically. The graphical description is a popular way to describe the solution of the Mathieu equations and is shown for m/z 197 in Figure 1A and for the isotopes of Yb in Figure 1C. Each m/z has a triangular-like stability region in which any kind of DC and RF combination assigns a stable trajectory through the quadrupole. It is worth noting that all stability diagrams have a common overlap in the low mass region. As such, selecting a combination of DC and RF in the overlap region allows the transmission of several m/z simultaneously. To maintain unit mass resolution (peak width: 0.7 amu at 10% peak height), quadrupoles therefore operate RF/DC combinations which are located on a scan line truncating the stability diagrams in regions without overlap as shown in Figure 1A and C (red line). The position of the line determines the mass resolution and ion transmission which correlate inversely. Increasing the y intercept while maintaining the slope increases mass resolution but decreases ion transmission and vice versa. Changing the y intercept and the slope simultaneously allows manipulation of the mass bandpass for selected mass ranges and increases ion transmission (compare yellow scan lines in Figure 1A and C).[38] This analysis mode is further referred to as 'bandpass mode'. In this study, the gain of slope of the scan line were selected to transmit a mass range with a bandwidth between 8 and 9 amu.

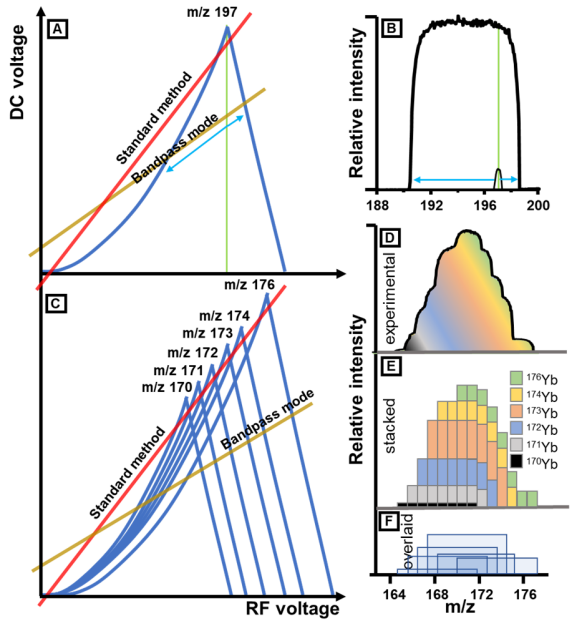

Figure 1 A: Schematic stability diagram for m/z 197. The scan line for standard operation (unit mass resolution) and for the bandpass mode are marked. **B:** Mass spectrum of Au using a standard scan line and the bandpass mode. **C:** Stability diagrams for all relevant Yb isotopes. Operating the bandpass mode results in a signal convolution. **D:** Yb mass spectrum recorded in bandpass mode. **E-F:** Simulated convolution of Yb isotope signals

Analysing a monoisotopic element like Au (^{197}Au) in bandpass mode has several observable effects as shown in Figure 1B. As the mass bandpass is increased to between 8 and 9 amu, sensitivity at 197 amu is increased by a factor of 8.4 due to improved ion transmission. In addition, the bandwidth expands further towards lower masses than higher masses when increasing the ion transmission (see arrows in Figure 1A and B). This asymmetry is a direct consequence of the non-symmetrical Mathieu stability diagram (compare Figure 1A, blue arrows and green line).

Analysing an element with several isotopes has additional effects when the bandpass is as large as 8 amu. Due to the increasing mass peak widths, isotopic signals start to overlap and convolute. Figure 1C shows a schematic stability diagram of all Yb isotopes with relevant abundances. Performing a standard quadrupole scan (red line Figure 1C) resolves each isotope. However, operating the bandpass mode (yellow line, Figure 1C) results on the one hand in an increase in the transmission of individual isotopes as previously shown for ^{197}Au, and on the other hand, in the convolution of isotopic signals which increases sensitivity further. Figure 1D shows the experimental mass spectrum of Yb in bandpass mode and Figure 1E and F show a simulation of how the different isotopes of Yb form one convoluted signal. Due to the asymmetry of the stability zone and mass peaks, signal convolution is also asymmetric and is more pronounced on the low mass side. The effect of signal convolution is pronounced for elements with several evenly abundant isotopes like Gd, Er and Yb. Figure 2 shows the mass spectra of Gd, Er, Yb and Au operating standard parameters and compares sensitivities as a measure of ion transmission and mass resolution against a method with increased ion extraction and operating the quadrupole in bandpass mode. The sensitivity of the monoisotopic Au (^{197}Au) increased 8.4-fold relative to the standard method. Gd, Er and Yb are lanthanides which have a broad isotope distribution as shown in Figure 2 (top). In standard quadrupole mass filtering, only one isotope at a time and therefore only a fraction of the total elemental ions of these elements is transmitted per dwell time, which limits sensitivity. In contrast, operating the quadrupole with a larger mass bandwidth increased sensitivity due to convoluted isotope signals. Highest intensities were obtained at 155 amu for Gd, 165 amu for Er and 171 amu for Yb, respectively. However, due to spectral overlap

of isotopes from Yb and Er, 172 amu and 163 amu were monitored to determine the relative improvement in sensitivity and later for SP ICP-MS. The bandpass mode increased sensitivities 33, 12 and 28-fold for Gd, Er and Yb relative to the standard method. Table 2 shows the factors of improvements after optimising ion extraction and transport and operating the bandpass mode, respectively.

The bandpass mode demonstrated potential to improve the figures of merits for elements with several isotopes unlikely to be confounded by spectral interferences. Gd, Er and Yb are critical elements for the photon upconversion in UCNPs and are incorporated into the $NaYF_4$ host structure by replacing Y^{3+}. UCNPs can also be analysed by targeting Y. While for Gd, Er and Yb confounding interferences are rather unlikely, the monoisotopic ^{89}Y is a 4d element for which interferences become more relevant. Depending on the matrix and the plasma conditions, decreasing mass resolution can result in adverse figures of merit if targeted masses are close to the mass range of ubiquitous elements (e.g. Sr) and prominent spectral interferences (e.g. Ar_2^+). Therefore, the bandpass mode was only applied to the analysis of Gd, Er, Yb and Au, while Y was analysed with optimised extraction and transport conditions increasing sensitivity by factor 4.2 (Table 2).

Analysis of Au NPs

Stable dispersions of Au NPs are frequently investigated in various matrices which makes them excellent model systems for method development and subsequent comparison. The detection of Au in ICP-MS is hampered by its high first ionisation potential which leads to low ion population within the plasma and restricts the sDL for single particle detection. To differentiate a NP signal with reasonable certainty from the noise and ionic background signals, NP signals must be significantly higher (>3 times) than the standard deviation of the background signal. Typically, NP dispersions are not monodisperse but have characteristic size distributions where fit functions were often used to describe and compare the distributions and maxima. Signal distributions that are interfered by background signals, can only be partially fitted, or require extrapolation.

Figure 3 A1 shows the signal distribution following the analysis of a 10.9 nm (±1 nm) Au NP dispersion employing a standard

Table 2. Relative sensitivities obtained for Y, Gd, Er, Yb and Au. For the standard method and optimised ion lenses method, the most abundant lanthanide isotopes (^{158}Gd, ^{166}Er and ^{174}Yb) were monitored. For the bandpass mode, higher sensitivities were achieved monitoring Gd at 155 amu, Er at 163 amu and Yb at 172 amu. All methods monitored ^{197}Au and ^{89}Y. Values are relative to a standard method for SP ICP-MS.

Element	Optimised ion lenses (Sensitivity relative to standard method)	Bandpass mode (Sensitivity relative to standard method)
Y	4.2	-
Gd	2.0	33
Er	1.4	12
Yb	2.4	28
Au	3.0	8.4

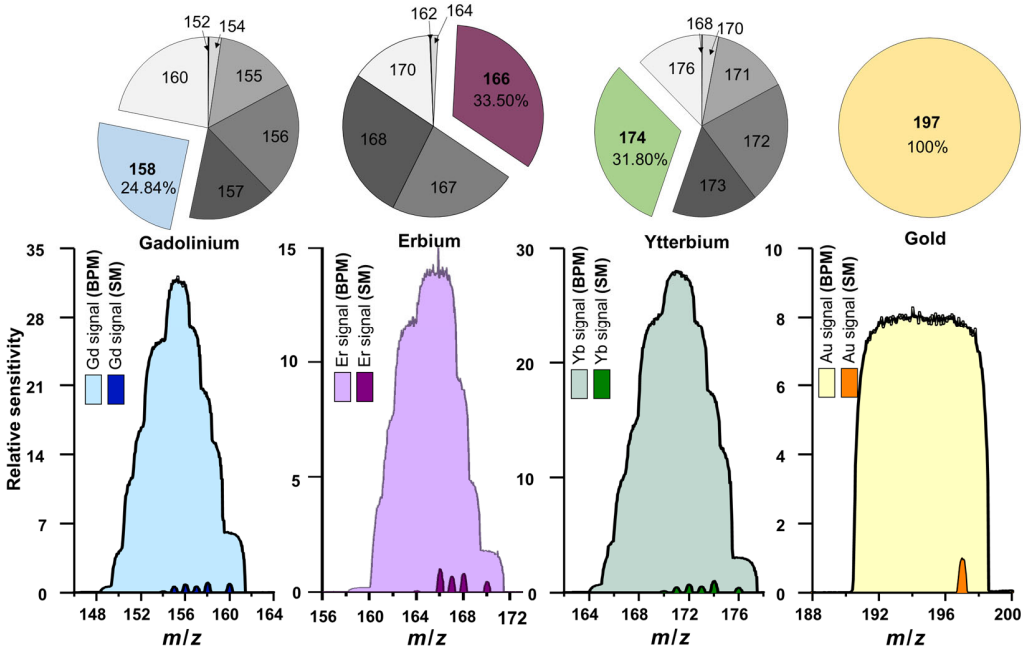

Figure 2. The elements **Gd**, **Er**, **Yb** and **Au** were analysed in standard (SM) and bandpass mode (BPM) to compare mass resolution and sensitivity. Ion transmission in bandpass mode was increased by two mechanisms: First the quadrupole transmission of individual isotopes was enhanced, exemplified by the monoisotopic **Au**. Second, transmission was further increased by the simultaneous acquisition of several isotopes as shown for **Gd, Er** and **Yb**.

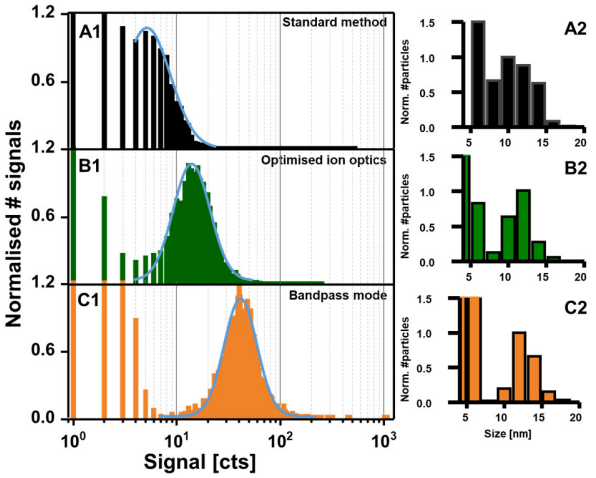

Figure 3. Analysis of a 10.9 nm Au NP dispersion. A standard method for SP ICP-MS (**A1-2**) is compared to a method with modified ion extraction and transport (**B1-2**). Operating the quadrupole additionally in bandpass mode allows background free NP detection (**C1-2**).

method (compare table 1 for instrumental parameters). While a maximum in the NP signal distribution corresponding to the mean NP diameter could be resolved, lower NP diameters were not distinguishable from background signals. Figure 3A2 shows the size distribution demonstrating interference of background signals with the size calculation. In this case particles detected with sizes below the mean diameter were comprised of signals originating from both background and NPs. The sDL was determined to be 7.0 nm. The optimisation of ion extraction and transport increased transmission and translated into improved signal to noise ratios as shown in Figure 3 B1 resulting in the improved differentiation of signals originating from Au NPs from background, which comprised of ions and noise. The improvement of the signal and noise ratio decreased the sDL from 7.0 nm to 4.7 nm. The corresponding size distribution is displayed in Figure 3 B2. Further improvement was evident in bandpass mode, which allowed complete resolution of Au NP signals from the ionic background and noise. This background free detection of Au NP signals is shown in Figure 3 C1 and resulted in higher accuracy of determined size distributions as shown in Figure 3 C1-2. As also shown in Figure 3, increasing the mass bandwidth increased the sensitivity for m/z 197 by a factor of 8.4. However, it needs to be considered that increasing the mass bandpass may have adverse effects on the background. Increasing noise concomitantly with ion transmission can therefore limit the improvement of signal to noise ratios. To monitor the effect of increasing transmission and mass bandpass on the background noise, a blank solution was analysed, and the signal standard deviation was determined as a measure of noise. Values of 0.36, 0.46 and 0.83 cts were calculated for the standard method, the method with optimised ion optics and the bandpass mode, respectively. The improvement in the signal to noise ratio achieved with the bandpass mode was therefore 3.7. The sDL were estimated to be 4.2 nm according to Lee *et al.*[42]. The analysis of smaller Au nanoclusters is discussed in the supplementary information. The sDL for all elements and all methods are shown in Table 3.

It was apparent that increasing ion transmission improved the sDL by enhancing signal to noise ratios allowing characterisation of small Au NPs. Application of the method to other types of nanoparticles must consider potential spectral interferences, the ionic background and background noise when increasing ion transmission, as the sDL is ultimately defined via the signal to noise ratio. Specifically, elements located in mass ranges where other elements are potentially interfering or likely to form polyatomic interferences (e.g., Y, Zn and Fe) should be investigated with great care.

Characterisation of UCNPs

The properties of UCNPs depend largely on their size, dispersity, elemental composition, and stoichiometry as well as on their stability, their tendency to aggregate and to undergo species transformation. As such, the characterisation of UCNPs requires versatile methods. However, the analysis by SP ICP-MS is limited due to small particle sizes and low mass fractions of elements with broad isotope distributions.

Optimising ion extraction and transport and using the bandpass mode has potential to improve sDL and to bring UCNPs within reach of SP ICP-MS. As a proof of concept, UCNPs with various diameters and elemental mass fractions were investigated; **Type I** was a 90 nm $NaYF_4$ host structure in which 20% and 2% of Y lattice positions were substituted by Yb and Er, respectively; **Type II** was a 20 nm sized $NaYF_4$ host structure in which 20% and 1% of Y lattice positions were replaced by Yb and Er, respectively; and **Type III** was a 15 nm $NaGdF_4$ host structure in which 20% and 2% of the Gd lattice positions were replaced by Yb and Er, respectively.

Figure 4 shows the Yb signal distribution of the **Type II** UCNP dispersion clearly showing the limitations of standard methods to provide background free detection of small particles with low elemental mass fractions. Although the standard method did detect UCNP signals that were statistically distinguishable from the background (Figure 4A), the smaller particles were confounded by the background. Modifying the ion lenses improved transmission and consequently the detection of individual UCNPs but did not provide background free detection (Figure 4B). For both signal distributions, neither Gaussian (not shown) nor log-normal (blue curve) functions provided an adequate fit. Figure 4C featuring the operation of the bandpass mode shows several maxima in the signal distributions which resulted from aggregation and the simultaneous detection of 2 or more particles. As such, these distributions could not be resolved with standard methods and could therefore not be modelled with a simple Gaussian or log-normal function. The bandpass mode was therefore critical to resolve signal distributions that resulted from the simultaneous detection of two or more particles and may be utilised to describe particle-particle interactions as discussed later. As before, increasing ion transmission also increased background noise. The standard deviation of the background for lanthanides increased from 0.06 cts for a standard method to 0.28 cts and 0.59 cts for the methods with

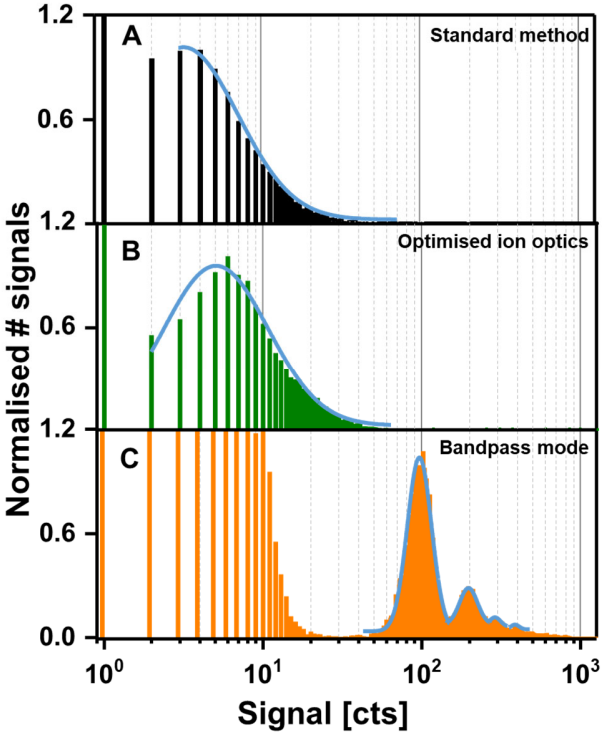

Figure 4. Yb signal distribution following singe particle analysis of dispersed 20 nm UCNPs ($NaYF_4$: 20%Yb, 1%Er, **type II**) using a standard method for SP ICP-MS (**A**). Particle registration was improved after optimising ion extraction and transport (**B**). The bandpass mode (**C**) allowed background free detection of individual UCNPs and resolved several maxima corresponding to aggregated UCNPs.

optimised ion optics and bandpass mode. Analysing Y with optimised ion optics increased the background noise from 0.37 cts to 0.93 cts.

The rapid sequential acquisition of several thousand NPs per minute was sufficient to construct statically representative models of size distributions of dispersed particles. Figure 5 shows the detection and characterisation of the three types of UCNPs. The **type I** UCNP dispersion contained particles with mean sizes of 90 nm and consisted of a $NaYF_4$ host structure that was doped with Yb (theoretical doping degree: 0.2) and Er (theoretical doping degree 0.02). Employing the high transmission methods provided background free acquisition of signals from Y, Yb and Er for individual NPs as shown in Figure 5A1-3. The targeting of various elements incorporated in UCNPs allowed determination of the stoichiometry and size distributions from different data sets as shown in Figure 5B1-3. Log-normal fit functions were used to find the first maxima of the signal distributions, which were subsequently used to determine the stoichiometry (0.79 Y: 0.181 Yb: 0.029 Er (Figure 5 C)) considering the response of ionic elemental standards for ICP-MS. The **type II** UCNP dispersion consisted of a 20 nm $NaYF_4$ host structure doped with Yb (theoretical doping degree 0.2) and Er (theoretical doping degree 0.01). Modification of ion extraction and transport and increasing the mass bandwidth were essential to resolve signal distributions shown in Figure 5D1-2. Due to the small diameters and low mass fraction, the doped Er was not observed for particles smaller than 25.3 nm and only Y and Yb were further considered for size distributions (Figure 5E1-2). Figure 5F shows the experimental ratio of Y and Yb (0.79:0.21). The **type III** 15 nm UCNPs ($NaGdF_4$ doped with Yb and Er) signal distributions are shown in Figure 5G1-2. The optimisation of ion transmission was again essential to resolve the first signal distribution maximum. The experimental ratio of Gd and Yb was 0.776: 0.224 as shown in Figure 5I (theoretical value: 0.8 Gd: 0.2Yb: 0.02 Er) and size distributions are shown in Figure 5H1-2. The sDLs for each elements, method and particle type are shown in Table 3. For the analysis of UCNP which contain Gd and Yb (e.g., type III UCNPs), oxide rates may impact accuracy. The Gd oxide rate was calculated by analysing a 1 ng/g ionic Gd solution and the oxide rate was found to be 1.8% (Figure S4). The impact of GdO on the Yb was calculated and subtracted.

Poisson model for UCNP interactions

Most of the UCNPs had two or more maxima in the signal distributions corresponding to the detection of two or more particles simultaneously. For an ideal NP dispersion with a sufficiently high particle concentration and no particle-particle interactions, the detection of none, one, or more particles may be described with the Poisson distribution.[46] Deviations from this distribution may be used to make an assessment about particle interactions, such as aggregation. Consider the type **II** UCNP dispersion (Figure 4C). Here, the dispersion was freshly diluted by a factor of $3x10^6$ and 0.525 ml were sampled. Overall, 37,862 particles were detected, of which 12,891 particles were registered individually. The high particle number concentration was chosen to demonstrate the utility of the Poisson statistics to predict the coincidental detection of two or more particles and for the comparison against a system that shows particle-particle interaction. The average signal duration of each signal was

Table 3. Size detection limits (sDLs) [nm] for Y, Gd, Er, Yb and Au for all types of NPs analysed. Y was analysed employing a method optimising ion lenses (OIL). Lanthanides were analysed employing the bandpass mode (BPM). For comparisons, the sDL for Au was also determined with a standard SP ICP-MS method (SM).

	Y	Gd	Er	Yb	Au
Au NP	-	-	-	-	SM: 7.0 OIL: 4.7 BPM:4.2
Type I UCNP	OIL: 13.6	-	BPM: 20.1	BPM: 12.2	-
Type II UCNP	OIL: 13.6	-	BPM: 25.3	BPM: 12.2	-
Type III UCNP	-	BPM: 5.7	BPM: 20.1	BPM: 12.2	-

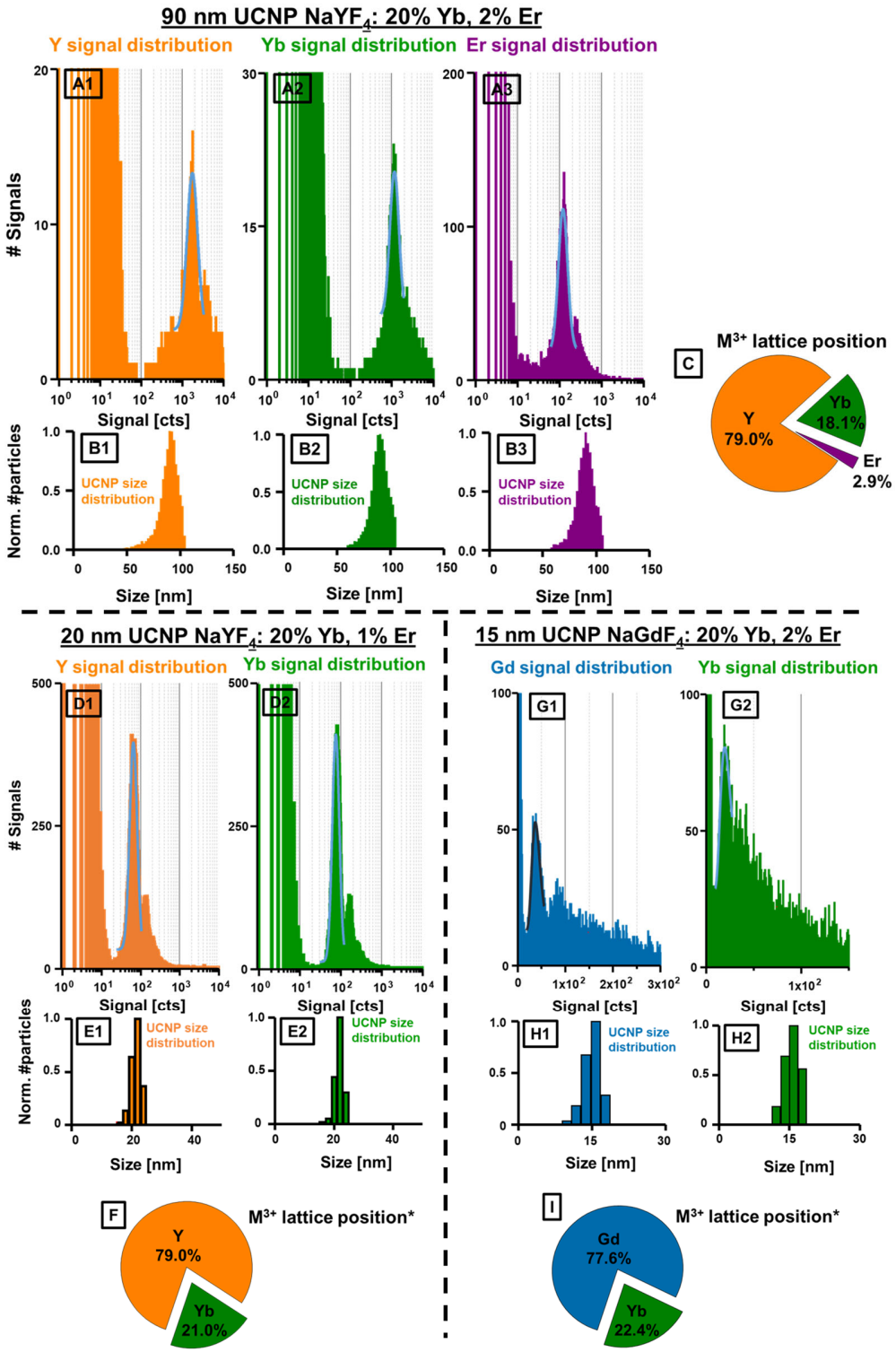

Figure 5. SP ICP-MS analysis of three types of UCNPs. The type **I** (**top, A-C**) consisted of a $NaYF_4$ host structure doped with 20% Yb and 2% Er. The type **II** (**bottom left, D-F**) consisted of a $NaYF_4$ host structure doped with 20% Yb and 1% Er. Type **III** (**bottom right, G-I)** consisted of a $NaGdF_4$ host structure doped with 20% Yb and 2% Er. The signal distributions for each type of UCNP and targeted elements are shown in **A, D** and **G,** respectively. Calibration allowed determination of the corresponding particle sizes as shown in **B**, **E** and **H**. The experimental molar ratios of targeted elements in detected UCNPs are shown in **C**, **F** and **I**. *For **type II** and **III**, Er was not detected and was not further considered.

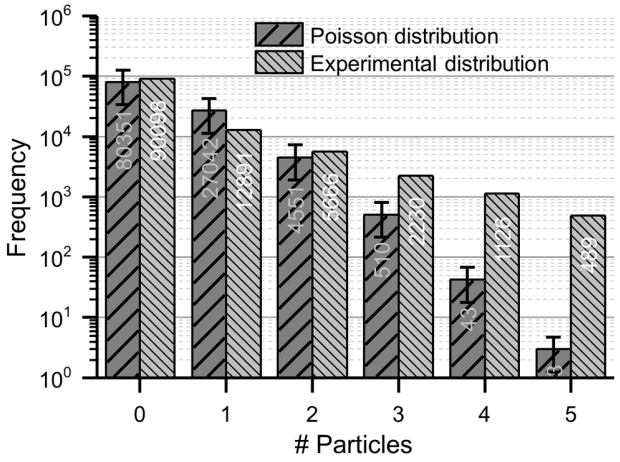

Figure 6. Comparison of the Poisson model and experimental results for detected UCNPs.

400 µs (±19%) and the total acquisition time was 90 s. Based on these data the Poisson distribution was calculated with a variance 0.3366 and is shown in Figure 6. From this model, it would be expected to detect no particle(s) in 71.4%, 1 particle in 24%, 2 particles in 4%, and 3 particles in 0.45% of all detection intervals. The detection of 4 and 5 particles are rather unlikely with 0.038% and 0.0026%, respectively (Table S1). However, in SP ICP-MS, no particles were detected in 80.1%, individual particles in 11.5%, 2 particles in 5% and 3 particles in 2% of all detection intervals. Furthermore, 4 and 5 particles were registered in 1.0% and 0.4% of detection intervals, respectively. Comparing the Poisson distribution with these experimental results, the detection of one individual particle occurred less frequently (0.48x) and the detection of two particles occurred more frequently (1.25x) than predicted by the Poisson distribution. However, the frequencies were within the model's standard deviation. Significantly increased frequencies were detected for three or more particles. The detection of 3, 4 and 5 particles occurred 4.4x, 26.2x and 169x more frequently, respectively, than predicted by the Poisson model and were outside the model's standard deviation. The deviation from the Poisson distribution may be explained by particle-particle interactions that favour aggregation. Deviations from the Poisson model can therefore be used to make an assessment about time dependent stability of dispersions in various matrices and solvents, which is an important factors for the utility of UCNPs in bio-sensing, deep-tissue optical bio-imaging and diagnostic techniques. The Poisson model further provides insight for method optimisation, for example, increasing the dilution factors to decrease aggregation and coincidental detection of NPs. Additional details on the Poisson statistics are given in the supplementary information.

CONCLUSION

This work presented novel approaches to optimise ion transmission in SP ICP-MS for the analysis of small diameter and low mass fraction NPs. Increasing the mass bandwidth of the quadrupole mass filter resulted in a decreased mass resolution and increased ion transmission providing sDL as small as 4.2 nm for Au NPs and allowing the background free size characterisation of a 10.9 nm (±1 nm) Au NP dispersion.

The developed methods were critical for the individual detection of UCNPs and analysis of a variety of elements incorporated in these particles. Depending on mass, background equivalent concentrations, isotopic abundances and spectral interferences, some elements required careful selection of transmission parameters. Y was confounded by spectral interferences and was therefore monitored with conventional quadrupole mass filtering and optimised ion extraction and transport parameters achieving sDL as low as 13.6 nm. The bandpass mode improved the sensitivity for Gd, Er and Yb substantially, providing sDL as low as 5.7, 20.1 and 12.2 nm for the targeted UCNP compositions. This enabled the accurate characterisation of size distributions and particle doping degrees. A Poisson model was developed to describe the aggregation of dispersed particles.

The presented methods improved the detection of small or low mass fraction NPs, and characterised UCNPs by SP ICP-MS for the first time. They can easily be adapted to the analysis of other NPs and have the potential to be used to study species transformation, particle number concentration, aggregation behaviour, doping degrees, and longitudinal stability.

AUTHOR CONTRIBUTIONS

The manuscript was written through contributions of all authors. All authors have given approval to the final version of the manuscript.

*Corresponding author:
David Clases, David.Clases@uts.edu.au

ACKNOWLEDGEMENTS

D.C. is funded by the Deutsche Forschungsgemeinschaft (DFG. German Research Foundation) – 417283954. X.X. is supported by the Chancellor Postdoctoral Research Fellowship of University of Technology Sydney. P.A.D is recipient of an Australian Research Council Discovery Project (DP190102361).

CONFLICT OF INTEREST

The authors declare no conflicts of interest.

REFERENCES

(1) Kolahalam, L. A.; Kasi Viswanath, I. V; Diwakar, B. S.; Govindh, B.; Reddy, V.; Murthy, Y. L. N. *Mater. Today Proc.* **2019**, *18*, 2182–2190.

(2) Gao, J.; Xu, B. *Nano Today* **2009**, *4* (1), 37–51.

(3) Fernandez-Fernandez, A.; Manchanda, R.;

McGoron, A. J. *Appl. Biochem. Biotechnol.* **2011**, *165* (7), 1628–1651.

(4) Jeevanandam, J.; Barhoum, A.; Chan, Y. S.; Dufresne, A.; Danquah, M. K. *Beilstein J. Nanotechnol.* **2018**, *9*, 1050–1074.

(5) Mourdikoudis, S.; Pallares, R. M.; Thanh, N. T. K. *Nanoscale* **2018**, *10* (27), 12871–12934.

(6) Du, Z.; Gupta, A.; Clarke, C.; Cappadona, M.; Clases, D.; Liu, D.; Yang, Z.; Karan, S.; Price, W. S.; Xu, X. *J. Phys. Chem. C* **2020**.

(7) Liu, Y.; Wang, F.; Lu, H.; Fang, G.; Wen, S.; Chen, C.; Shan, X.; Xu, X.; Zhang, L.; Stenzel, M.; Jin, D. *Small* **2020**, *16* (6), 1905572.

(8) Zhou, J.; Sun, Y.; Du, X.; Xiong, L.; Hu, H.; Li, F. *Biomaterials* **2010**, *31* (12), 3287–3295.

(9) Ma, D.; Shen, Y.; Su, T.; Zhao, J.; Rahman, N. U.; Xie, Z.; Shi, F.; Zheng, S.; Zhang, Y.; Chi, Z. *Mater. Chem. Front.* **2019**, *3* (10), 2058–2065.

(10) Hao, S.; Shang, Y.; Li, D.; Ågren, H.; Yang, C.; Chen, G. *Nanoscale* **2017**, *9* (20), 6711–6715.

(11) Generalova, A. N.; Chichkov, B. N.; Khaydukov, E. V. *Adv. Colloid Interface Sci.* **2017**, *245*, 1–19.

(12) Wang, M.; Abbineni, G.; Clevenger, A.; Mao, C.; Xu, S. *Nanomedicine Nanotechnology, Biol. Med.* **2011**, *7* (6), 710–729.

(13) Liu, Y.; Lu, Y.; Yang, X.; Zheng, X.; Wen, S.; Wang, F.; Vidal, X.; Zhao, J.; Liu, D.; Zhou, Z.; Ma, C.; Zhou, J.; Piper, J. A.; Xi, P.; Jin, D. *Nature* **2017**, *543* (7644), 229–233.

(14) Chen, G.; Qiu, H.; Prasad, P. N.; Chen, X. *Chem. Rev.* **2014**, *114* (10), 5161–5214.

(15) Li, X.; Zhang, F.; Zhao, D. *Chem. Soc. Rev.* **2015**, *44* (6), 1346–1378.

(16) Gee, A.; Xu, X. *Surfaces* **2018**, *1* (1), 96–121.

(17) Pröfrock, D.; Prange, A. *Appl. Spectrosc.* **2012**, *66* (8), 843–868.

(18) Clases, D.; Sperling, M.; Karst, U. *Trends Anal. Chem.* **2018**, *104*, 135–147.

(19) Bishop, D. P.; Hare, D. J.; Clases, D.; Doble, P. A. *TrAC - Trends in Analytical Chemistry*. 2018, pp 11–21.

(20) Soto-Alvaredo, J.; Montes-Bayón, M.; Bettmer, J. *Anal. Chem.* **2013**, *85* (3), 1316–1321.

(21) Meermann, B.; Nischwitz, V. *J. Anal. At. Spectrom.* **2018**, *33* (9), 1432–1468.

(22) González de Vega, R.; Clases, D.; Fernández-Sánchez, M. L.; Eiró, N.; González, L. O.; Vizoso, F. J.; Doble, P. A.; Sanz-Medel, A. *Anal. Bioanal. Chem.* **2019**, *411* (3), 639–646.

(23) Metarapi, D.; Šala, M.; Vogel-Mikuš, K.; Šelih, V. S.; van Elteren, J. T. *Anal. Chem.* **2019**, *91* (9), 6200–6205.

(24) Strenge, I.; Engelhard, C. *J. Anal. At. Spectrom.* **2020**, *35* (1), 84–99.

(25) Álvarez-Fernández García, R.; Corte-Rodríguez, M.; Macke, M.; LeBlanc, K. L.; Mester, Z.; Montes-Bayón, M.; Bettmer, J. *Analyst* **2020**, *145* (4), 1457–1465.

(26) Meermann, B.; Laborda, F. *J. Anal. At. Spectrom.* **2015**, *30* (6), 1226–1228.

(27) Franze, B.; Strenge, I.; Engelhard, C. *J. Anal. At. Spectrom.* **2017**, *32* (8), 1481–1489.

(28) Mozhayeva, D.; Engelhard, C. *J. Anal. At. Spectrom.* **2020**.

(29) Flores, K.; Turley, R. S.; Valdes, C.; Ye, Y.; Cantu, J.; Hernandez-Viezcas, J. A.; Parsons, J. G.; Gardea-Torresdey, J. L. *Appl. Spectrosc. Rev.* **2019**, 1–26.

(30) Sötebier, C. A.; Kutscher, D. J.; Rottmann, L.; Jakubowski, N.; Panne, U.; Bettmer, J. *J. Anal. At. Spectrom.* **2016**, *31* (10), 2045–2052.

(31) Tuoriniemi, J.; Cornelis, G.; Hassellöv, M. *J. Anal. At. Spectrom.* **2015**, *30* (8), 1723–1729.

(32) Peters, R.; Herrera-Rivera, Z.; Undas, A.; Van Der Lee, M.; Marvin, H.; Bouwmeester, H.; Weigel, S. *J. Anal. At. Spectrom.* **2015**, *30* (6), 1274–1285.

(33) Mozhayeva, D.; Engelhard, C. *J. Anal. At. Spectrom.* **2019**, *34* (8), 1571–1580.

(34) Montaño, M. D.; Olesik, J. W.; Barber, A. G.; Challis, K.; Ranville, J. F. *Anal. Bioanal. Chem.* **2016**, *408* (19), 5053–5074.

(35) Fréchette-Viens, L.; Hadioui, M.; Wilkinson, K. J. *Talanta* **2019**, *200*, 156–162.

(36) Balcaen, L.; Woods, G.; Resano, M.; Vanhaecke, F. *J. Anal. At. Spectrom.* **2013**, *28* (1), 33–39.

(37) Bishop, D. P.; Clases, D.; Fryer, F.; Williams, E.; Wilkins, S.; Hare, D. J.; Cole, N.; Karst, U.; Doble, P. A. *J. Anal. At. Spectrom.* **2016**, *31* (1), 197–202.

(38) Clases, D.; Gonzalez de Vega, R.; Funke, S.; Lockwood, T. E.; Westerhausen, M.; Taudte, R. V.; Adlard, P. A.; Doble, P. *J. Anal. At. Spectrom.* **2020**, *35*, 728–735.

(39) Liu, D.; Xu, X.; Du, Y.; Qin, X.; Zhang, Y.; Ma, C.; Wen, S.; Ren, W.; Goldys, E. M.; Piper, J. A.; Dou, S.; Liu, X.; Jin, D. *Nat. Commun.* **2016**, *7*, 10254.

(40) Wang, F.; Deng, R.; Liu, X. *Nat. Protoc.* **2014**, *9* (7), 1634–1644.

(41) Mackenzie, L. E.; Goode, J. A.; Vakurov, A.; Nampi, P. P.; Saha, S.; Jose, G.; Millner, P. A. *Sci. Rep.* **2018**, *8* (1), 1–11.

(42) Lee, S.; Bi, X.; Reed, R. B.; Ranville, J. F.; Herckes, P.; Westerhoff, P. *Environ. Sci. Technol.* **2014**, *48* (17), 10291–10300.

(43) Clases, D.; Ueland, M.; Gonzalez de Vega, R.; Doble, P.; Pröfrock, D. *Talanta* **2021**, *221*, 121424.

(44) González-Gago, A.; Pröfrock, D.; Prange, A. *J. Anal. At. Spectrom.* **2015**, *30* (1), 180–190.

(45) Clases, D.; Gonzalez de Vega, R.; Funke, S.; Lockwood, T. E.; Westerhausen, M. T.; Taudte, R. V.; Adlard, P. A.; Doble, P. A. *J. Anal. At. Spectrom.* **2020**, *35* (4), 728–735.

(46) Olesik, J. W.; Gray, P. J. *J. Anal. At. Spectrom.* **2012**, *27* (7), 1143–1155.